On-line harmonic signal denoising from the measurement with non-stationary and non-Gaussian noise

Liang Yu [a], Yanqi Chen [b], Yongli Zhang [c], Ran Wang [c,*], Zhaodong Zhang [b]

[a] *Instutute of Vibration, Shock and Noise, State Key Laboratory of Mechanical System and Vibration, Shanghai Jiao Tong University, Shanghai, 200240, China*
[b] *Hagong Intelligent Robot Co.Ltd, Shanghai, 201100, China*
[c] *College of Logistic Engineering, Shanghai Maritime University, Shanghai, 201306, China*

ARTICLE INFO

ABSTRACT

Harmonic denoising is one of the important preprocessing steps before extracting harmonic signal characteristics. Several signal processing techniques have been developed and applied for denoising the harmonics, which assume that the noise follows a Gaussian distribution and is stationary. However, the noise is often not so simple as a Gaussian distribution, and it could be non-Gaussian and non-stationary in most practical scenarios. A novel online denoising method for the harmonic signal with non-stationary complex noises based on the Bayesian Maximum a Posteriori (MAP) framework is proposed in this paper. The measured signal is divided equally into several frames. Then these frames are transformed into the time-frequency domain by the Short-Time Fourier transform (STFT) and are assumed to be the sum of a low-rank matrix and a noise matrix. The online model of the low-rank matrix and the noise matrix is then constructed between the frames. The online Gaussian mixture model (GMM) and low-rank matrix factorization are performed on the measurement matrix in the complex number domain to reconstruct the harmonic signal. The performance of the proposed method is validated in the simulations. The non-Gaussian and non-stationary noise can be removed more effectively, and the proposed algorithm can improve the frequency estimation accuracy.

© 2022 Elsevier B.V. All rights reserved.

1. Introduction

Harmonic signals exist in many scenarios, such as mechanical condition monitoring [1,2], helicopter detection [3,4], speech acquisition [5–7], biomedical diagnosis [8], etc. Noise is inevitable in the measurement process. For example, the most important step in helicopter detection is to detect the harmonic signals generated by the rotor. However, there will be wind, environmental, and equipment measurement noise, making it difficult to extract target information. Especially when the signal-to-noise (SNR) ratio is low, it is challenging to perform feature extraction or fundamental frequency estimation [9,10] on harmonic signals. Therefore, it is essential to denoise the measurement before the signal is characterized.

During the past decades, many harmonic signal denoising techniques have been developed and applied, including Kalman filter [11–13], spectral subtraction [14,15], wavelet transform (WT) [16–18], singular value decomposition (SVD) [19,20], and fast orthogonal search (FOS) [21]. The Kalman filter is based on second-order statistics and can suppress the noise, but the performance of processing the impulsive noise is not as good as the performance of processing the additive Gaussian noise [22,23]. Spectral subtraction (SS) [15] is a widely used method. The noise-free signal is extracted from the noisy measurement by modeling the statistical spectrum characteristics of the noise in advance and then the noise spectrum can be subtracted. One of the disadvantages of the Spectral Subtraction method is that the background noise is assumed to be statistically smooth.

The time-domain denoising method based on the Hankel matrix [19,20] with Gaussian noise assumption is also one of the classical denoising methods. The Hankel matrix of a harmonic signal has the low-rank property, and its rank is equal to the number of harmonics. The denoising problem for the harmonic signal can be regarded as the low-rank matrix factorization (LRMF) for the Hankel matrix. Singular value decomposition (SVD) is one of the more commonly used methods for the low-rank reconstruction of the Hankel matrix. The shortcoming of SVD is that the computational efficiency deteriorates when the matrix dimension is too large. The

---

* Corresponding author.
 E-mail address: ranwang@shmtu.edu.cn (R. Wang).

random SVD [24] combined with soft thresholding is used to solve the problem of huge data volume. Besides, The reweighted SVD [25] is proposed to address the fact that traditional SVD would ignore singular value components with small replication but valuable features.

The abovementioned algorithms are mainly based on the noise following a Gaussian distribution.

However, more complex noise components are found in practical application scenarios, leading to simple Gaussian noise assumptions that are no longer satisfactory. The denoising methods based on non-Gaussian noise assumptions are then developed and applied. The method using particle filters [26] is presented for denoising signals in a non-Gaussian environment. Two different state-space models based on Fourier coefficients and Gabor coefficients are built for harmonic estimation. The effectiveness of the algorithm is verified in the simulation for the alpha-stable and Rayleigh distribution noises. The Gaussian Mixture Model (GMM) is also an effective model to fit the non-Gaussian noise [27]. GMM can theoretically fit an arbitrary distribution by adjusting the parameters and weights of the mixture of Gaussian distributions. The state estimation of non-Gaussian noise can also be improved by the improved Kalman filter based on the maximum correntropy criterion [28] using high-order statistics.

Moreover, some online algorithms are also developed to address the non-stationary properties of noises. The extended Gabor-Morlet wavelets [29] are adopted to approximate interference with time-varying properties. The online filtering scheme [30] is proposed based on smoothness priors and a constrained least-squares problem, which is more efficient than the traditional Tikhonov regularization and applicable to non-stationary scenarios. The non-stationary white noise is added to the electrocardiogram (ECG), and the algorithm is verified to reconstruct the signal efficiently. The particle filter [31] derived from a generalized likelihood function of GMM has also been shown to have good denoising performance for non-stationary noise, as long as the noise parameters do not vary too drastically.

The non-Gaussian noise can be fitted by the GMM very effectively, and the non-stationary noise can be solved well by the online model. The algorithm that combines these two principles can be further developed. To this end, a novel online denoising method has been proposed for the harmonic signal with non-stationary and non-Gaussian noise, which has two main innovations:

(1) The measurement is transformed from the original time domain into the high-dimensional time-frequency domain by STFT, and the complex-valued GMM is adapted to deal with the complexity of the noise. The problem of harmonic denoising is transformed into a problem of low-rank matrix reconstruction in the complex domain. In this way, the signal and the noise are estimated simultaneously from the two scales of frequency and time.

(2) An online algorithm based on the Bayesian Maximum a Posteriori (MAP) framework is proposed in this paper to deal with the non-stationary characteristics of the noise. The measurement is divided equally into many smaller intervals, and each is called a frame. The core idea is to use the information of the previous frame as the prior information of the subsequent frame and to denoise the next frame by maximizing the posterior function in the Bayesian framework. The time-varying GMM parameters and signal parameters are updated online through the Expectation-Maximization algorithm (EM).

The paper is organized as follows. The problem statement is described in Section2. The online model of harmonic signal with non-Gaussian and non-stationary noise is constructed in Section 3. Section 4 is the parameter estimation method performed through the Expectation-Maximization (EM) algorithm of an online GMM (OGMM) model. The simulation and verification of experimental
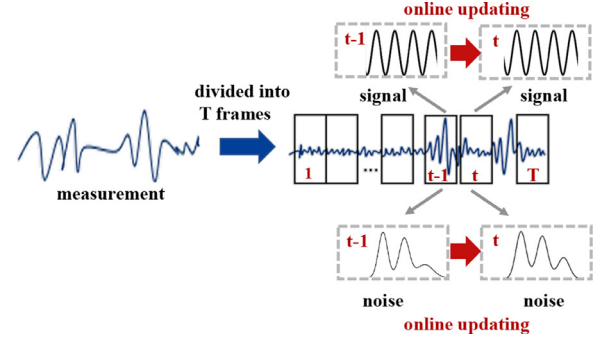
Fig. 1. The principle of the online algorithm. The discrete measurement time sequence is divided equally into T frames, which can be considered the sum of the signal and the noise. The information of the next frame can be learned from the previous frame, then the online updating method is established.

data are shown in Section 5. And a brief conclusion is drawn in Section 6.

2. Problem statement

A general model of the real-valued sinusoidal signal with noise can be expressed as:

$$p(n) = s(n) + e(n) = \sum_{k=0}^{N-1} X_k e^{ik\frac{2\pi}{N}n} + e(n), n = 0, \ldots, N, \qquad (1)$$

where $p(n)$ can be considered as the measurement, $s(n)$ is the noise-free signal, $e(n)$ is the noise, N denotes the number of sampling points, and X_k is the coefficient of the discrete Fourier transform (DFT) of an N-periodic sequence. The harmonic signal is focused on in this paper, so the additional assumption is made that most values of X_k are zero or negligible. $e(n)$ is generally assumed to be the Gaussian noise. However, the signal with non-Gaussian and non-stationary noise is considered in this paper. The first term, "non-Gaussian," describes the complicated statistical properties of the noise, which is not only the Gaussian distribution. The second term, "non-stationary," is used to describe that the statistical properties of the noise are time-varying.

The non-stationary characteristics of the noise are addressed first. It is necessary to introduce a variable on the time scale to deal with the non-stationary characteristics, and a common practice is to introduce the concept of frames. The discrete measurement time sequence is divided equally into T intervals, and an interval is called a frame, as shown in Fig. 1. The harmonic components are invariant between different frames, while the noise components are unstable. If the harmonic signal of each frame is characterized in a relatively stable form, the invariant components can be learned from the acquired signal. Many methods can describe the invariant characteristics of harmonic signals, such as DFT or STFT.

In addition, the subsequent frame can be updated online by transferring the information learned in the previous frame to the next. The online update method can reduce the amount of iterative calculation and may be used in real-time scenarios. The principle of the online model is shown in Fig. 1.

In this paper, the STFT is applied to characterize the invariant features of harmonic signals in each frame. More detailed information can be obtained by STFT in each frame compared with DFT. Moreover, STFT has an advantage in dealing with noises with non-stationary features. The harmonic signal in the time domain can be transformed into the time-frequency domain. The time-frequency matrix of each time signal can be obtained by performing the STFT
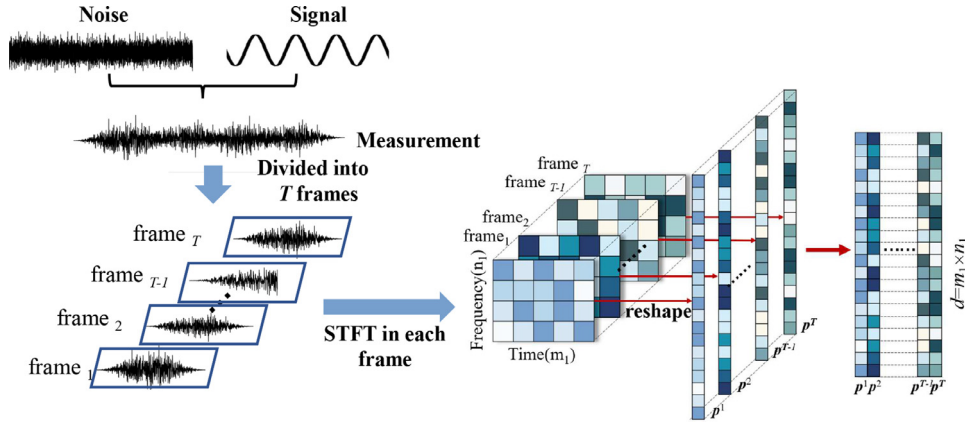
Fig. 2. The process of constructing the online model through a series of STFT matrices. The signal with N samples is uniformly divided into T frames, and then the STFT is conducted in each frame to transform the signal from the time domain to the time-frequency domain. The size of the time-frequency matrix for each frame depends on the time and frequency parameters in the STFT, which is assumed to be $n_1 \cdot m_1$ in the process. The signal in each frame is represented by an $n_1 \cdot m_1$ dimensional matrix. The time-frequency matrix of the tth ($t = 1, 2, \ldots, T$) frame is reshaped into a d-dimensional ($d = n_1 \cdot m_1$) complex-valued vector $\boldsymbol{p}^t$. The column vectors representing the time-frequency information from frame 1 to T are combined into the matrix.

[32] on the signal.

$$\text{STFT}_p(\tau, \omega) = \sum_{n=0}^{N-1} p(n + \tau)w[n]e^{-j\frac{2\pi}{N}\omega n}, \tag{2}$$

where STFT_p denotes the STFT matrix of the signal p regarding the time and frequency parameters, τ is the time parameter, ω is the frequency parameter, w is the windowing function and $e^{-j\frac{2\pi}{N}\omega n}$ is the basis function. The signal with N samples is uniformly divided into T frames, and then the STFT is conducted in each frame to transform the signal from the time domain to the time-frequency domain. The size of the time-frequency matrix for each frame depends on the time and frequency parameters (τ, ω) in the STFT, which is assumed to be $n_1 \cdot m_1$ in the process. The signal in each frame is represented by an $n_1 \cdot m_1$ dimensional matrix. Then the time-frequency matrix for each frame is reshaped into a d-dimensional ($d = m_1 \cdot n_1$) complex-valued column vector $\boldsymbol{p}^t$. The column vectors representing the time-frequency information from frame 1 to T are combined into a matrix. The construction process of the measurement matrix of the first T frame is shown in Fig. 2. The low-rank characteristics of the time-frequency matrix for the harmonic signals [33,34] have been proven that the rank of a complex-valued spectrogram depends on the number of sinusoids. So the low-rank matrix decomposition method is applied to extract the signal matrix.

The matrix $\boldsymbol{P}$ containing the first T frames is formed by the vector $\boldsymbol{p}^1, \ldots, \boldsymbol{p}^T$, and can be expressed as

$$\boldsymbol{P} = \boldsymbol{U}^T \boldsymbol{V} + \boldsymbol{E}, \tag{3}$$

where $\boldsymbol{P} = [\boldsymbol{p}^1, \ldots, \boldsymbol{p}^T] \in \mathbb{C}^{d \times T}$ is the time-frequency matrix, $\boldsymbol{U} \in \mathbb{C}^{r \times d}$, $\boldsymbol{V} \in \mathbb{C}^{r \times T}$ is the low rank factorization of the time-frequency matrix with $r \ll \min(d, T)$, and $\boldsymbol{E}$ denotes the noise matrix. The rank of the STFT matrix r can be thought of as being related to the number of harmonics, and the STFT matrix can be considered to have a low-rank property compared with the dimension of the matrix [24,33,34]. It is worth noting that the dimension of $\boldsymbol{U}$ is not related to frame number T. The two $\boldsymbol{U}$, $\boldsymbol{v}_j$ (the jth column vectors of $\boldsymbol{V}$) can be multiplied to obtain a column vector, which is composed of the time-frequency matrix of the jth frame.

Each element in $\boldsymbol{P}$ is

$$\boldsymbol{P}_{ij} = \boldsymbol{u}_i^T \boldsymbol{v}_j + \boldsymbol{e}_{ij}, \tag{4}$$

where $\boldsymbol{u}_i$ (the ith column vectors of $\boldsymbol{U}$) denotes the subspace vector of the data $\boldsymbol{P}_{ij}$, $\boldsymbol{v}_j$ (the jth column vectors of $\boldsymbol{V}$) represents the subspace coefficient vector of $\boldsymbol{P}_{ij}$, and $\boldsymbol{e}_{ij}$ represents the noise element

[35]. The notation *[X]* represents the probability density function (PDF) of a random variable *X*. The innovation in this paper is to model the noise by the Gaussian mixture model, which can approximate any continuous distribution. Each $\boldsymbol{e}_{ij}$ is assumed to be sampled from the GMM distribution:

$$[\boldsymbol{e}_{ij}] = \sum_{k=1}^{K} \pi_k N_{\mathbb{C}}(0, \sigma_k^2), \tag{5}$$

where $N_{\mathbb{C}}(\boldsymbol{e}_{ij}|0, \sigma_k^2)$ represents a Gaussian distribution with the mean of 0 and the variance of σ_k^2, π_k denotes the mixing weight ($0 \le \pi_k \le 1, \sum_{k=1}^{K} \pi_k = 1$). Then, the probability of $\boldsymbol{P}_{ij}$ can be expressed as

$$[\boldsymbol{P}_{ij}|\boldsymbol{u}_i, \boldsymbol{v}_j, \Pi, \Sigma] = \sum_{k=1}^{K} \pi_k N_{\mathbb{C}}(\boldsymbol{u}_i^T \boldsymbol{v}_j, \sigma_k^2), \tag{6}$$

where Π, Σ are the weight matrix and the variance matrix of the GMM, respectively.

The above settings (Eqs. (2)–(6), Figs. 1, and 2) describe the process of transforming the harmonic denoising problem into a low-rank subspace reconstruction problem: the time domain discrete signal is divided into frames, and STFT is performed on each frame; the STFT matrix of each frame is compressed into a column vector, and the column vectors of all frames are combined into a target matrix; the original signal is denoised by performing a low-rank decomposition of the target matrix with a GMM. Then the parameters can be solved by obtaining online update rules. Similar to the Retinex-based method [36,37], the proposed method in this paper first transforms the signal to a domain that can be easily separated from the interference and then to the original domain. However, it is worth noting that the problems discussed in this paper are still very different from image processing, both in terms of model construction, noise term modeling, and data types.

3. Online model for the low-rank signal matrix and the Gaussian mixture model for the noise

In this section, the method for building an online update model for the parameters, which is based on the low-rank model in Section 2, will be illustrated. Assuming that $\boldsymbol{p}^t$ is the latest frame along the time sequence, the parameters to be updated include the GMM noise parameters $\Pi^t = \{\pi_k^t\}_{k=1}^K$, $\Sigma^t = \{\sigma_{k,t}^2\}_{k=1}^K$ and the subspace parameters $\boldsymbol{U}^t, \boldsymbol{v}^t$. These four parameters need to be regularized under the previous knowledge $\Pi^{t-1}, \Sigma^{t-1}, \boldsymbol{U}^{t-1}, \boldsymbol{v}^{t-1}$ and the

observed signal $\boldsymbol{p}^t$ to construct an online model. The maximum a posteriori (MAP) principle is suited to solve this problem [38]. The likelihood function can be obtained from the current information $\boldsymbol{p}^t$ and the information of the first $t-1$ frames can be regarded as the prior function of the parameters, so the posterior function can be obtained. The purpose is to maximize the posterior function regarding $\boldsymbol{\Pi}^t = \{\pi_k^t\}_{k=1}^K$, $\boldsymbol{\Sigma}^t = \{\sigma_{k,t}^2\}_{k=1}^K$, $\boldsymbol{U}^t$, $\boldsymbol{v}^t$. It should be noted that the superscript t is shifted to the subscript in order to make the symbolic representation of the variance clearer, and this rule also applies to all symbols in this paper that have multiple superscripts.

The conjugate priors for the GMM parameters $\boldsymbol{\Sigma}^t$ and $\boldsymbol{\Pi}^t$ can be set as follows(the detailed derivation process is shown in the equations (A.1) and (A.2) in the Appendix A), which are the Inverse-Gamma and Dirichlet distributions, respectively:

$$\sigma_{k,t}^2 \sim \text{Inv} - \text{Gamma}\left(\frac{N_k^{t-1}-1}{2}, \frac{N_k^{t-1}\sigma_{k,t-1}^2}{2}\right), \tag{7}$$

$$\boldsymbol{\Pi}^t \sim \text{Dir}(\boldsymbol{\alpha}), \tag{8}$$

where $\boldsymbol{\alpha} = (N^{t-1}\pi_1^{t-1}+1,\ldots,N^{t-1}\pi_K^{t-1}+1)$, $N^{t-1} = \sum_{k=1}^K N_k^{t-1}$, $\pi_k^{t-1} = \frac{N_k^{t-1}}{N^{t-1}}$, N^{t-1} denotes the data amount in the $t-1$ frame, and N_k^{t-1} denotes the number of data from the kth Gaussian model in the $t-1$ frame. The parameters in these two distributions can be obtained from the likelihood functions from the first $t-1$ frames, which are derived in more detail in the Appendix. The parameters of the distributions carry the superscript $t-1$ as can be seen from Eqs. (7) and (8), which indicates that the information learned from the previous frames is introduced into the current frame.

For the low-rank subspace of the signal matrix, a Gaussian distribution prior is set for each row vector:

$$\boldsymbol{u}_i^t \sim N_{\mathbb{C}}\left(\boldsymbol{u}_i^{t-1}, \frac{1}{\rho}\boldsymbol{A}_i^{t-1}\right), \tag{9}$$

where $\frac{1}{\rho}\boldsymbol{A}_i^{t-1}$ is the covariance matrix and ρ can control the effect of the prior. The connection between $\boldsymbol{u}^t$ and $\boldsymbol{u}^{t-1}$ is built in this way. $[v]$ can be solved after the remaining parameters $\{\boldsymbol{\Pi}, \boldsymbol{\Sigma}, \boldsymbol{U}\}$ are determined, so there is no need to set a prior on $[v]$. The notation of $[v]$ in the following describtion is only for constructing a fully Bayesian model. The probabilistic graphical model of this online model is shown in Fig. 3.

All the parameters are denoted by $\boldsymbol{\Theta}^{t-1}$, the posterior distribution of $\{\boldsymbol{\Pi}, \boldsymbol{\Sigma}, v, \boldsymbol{U}\}$ can be derived in the following form:

$$[\boldsymbol{\Pi}, \boldsymbol{\Sigma}, v, \boldsymbol{U}|\boldsymbol{p}^t, \boldsymbol{\Theta}^{t-1}] \propto (\text{likelihood} \times \text{priori})$$
$$= [\boldsymbol{p}^t|\boldsymbol{\Pi}, \boldsymbol{\Sigma}, v, \boldsymbol{U}][\boldsymbol{\Pi}^t|\boldsymbol{\Theta}^{t-1}][\boldsymbol{\Sigma}^t|\boldsymbol{\Theta}^{t-1}][\boldsymbol{U}^t|\boldsymbol{\Theta}^{t-1}][v^t]. \tag{10}$$

The maximization of Eq. (10) can be transformed into the minimizing problem of Eq. (11) regarding $\{\boldsymbol{\Pi}, \boldsymbol{\Sigma}, v, \boldsymbol{U}\}$:

$$\mathcal{L}^t(\boldsymbol{\Pi}, \boldsymbol{\Sigma}, v, \boldsymbol{U}) = \ln([\boldsymbol{\Pi}, \boldsymbol{\Sigma}, v, \boldsymbol{U}|\boldsymbol{p}^t, \boldsymbol{\Theta}^{t-1}])$$
$$= -\ln([\boldsymbol{p}^t|\boldsymbol{\Pi}, \boldsymbol{\Sigma}, v, \boldsymbol{U}]) + R_F^t(\boldsymbol{\Pi}, \boldsymbol{\Sigma}) + R_B^t(\boldsymbol{U}), \tag{11}$$

where

$$\ln([\boldsymbol{p}^t|\boldsymbol{\Pi}, \boldsymbol{\Sigma}, v, \boldsymbol{U}]) = \sum_{i=1}^d \ln\left(\sum_{k=1}^K \pi_k^t N_{\mathbb{C}}(\boldsymbol{u}_i^{t^T} v^t, \sigma_k^2)\right), \tag{12}$$
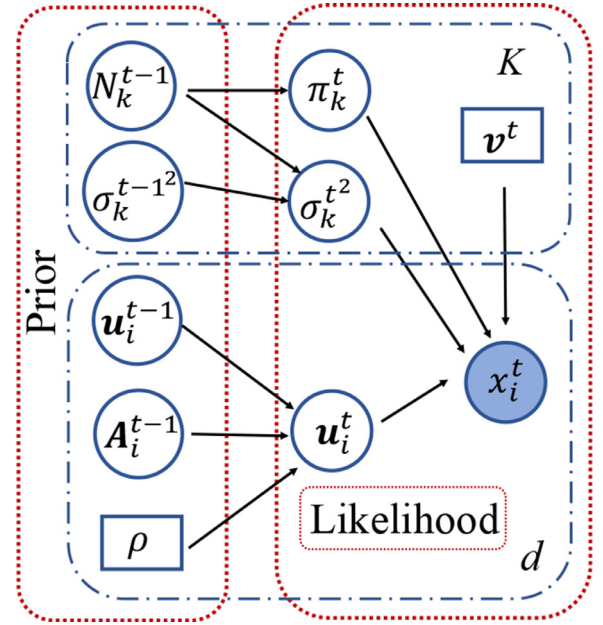

Fig. 3. The probabilistic graphical model for the OGMM algorithm. The circles and squares indicate variables, and the filled-in circles identify the observed data. K and d indicate the number of circled variable repetitions in the blue dotted box. The parameters inside the two red dashed boxes represent the prior parameters and the likelihood function. (For interpretation of the references to colour in this figure legend, the reader is referred to the web version of this article.)

$$R_F^t(\boldsymbol{\Pi}, \boldsymbol{\Sigma}) = \ln([\boldsymbol{\Pi}^t|\boldsymbol{\Theta}^{t-1}][\boldsymbol{\Sigma}^t|\boldsymbol{\Theta}^{t-1}])$$
$$= \sum_{k=1}^K N_k^{t-1}\left(\frac{\sigma_{k,t-1}^2}{2\sigma_{k,t}^2} + \ln\sigma_k\right) - N^{t-1}\sum_{k=1}^K \pi_k^{t-1}\ln\pi_k^t, \tag{13}$$

$$R_B^t(\boldsymbol{U}) = \ln([\boldsymbol{U}^t|\boldsymbol{\Theta}^{t-1}])$$
$$= \rho\sum_{i=1}^d (\boldsymbol{u}_i - \boldsymbol{u}_i^{t-1})^H(\boldsymbol{A}_i^{t-1})^{-1}(\boldsymbol{u}_i - \boldsymbol{u}_i^{t-1}). \tag{14}$$

The first term in Eq. (12) is the likelihood function of the current frame $\boldsymbol{p}^t$ under the learned parameters $\{\boldsymbol{\Pi}, \boldsymbol{\Sigma}, v, \boldsymbol{U}\}$. The second term in Eq. (13) is the regularization term for the noise distribution because it contains only $\{\boldsymbol{\Pi}, \boldsymbol{\Sigma}\}$. The relationship between the previous subspace vector and the current subspace vector is established in the third term in Eq. (14). The online model of the OGMM algorithm based on the MAP principle is built by the above derivation.

4. EM Algorithm for updating the low-rank subspace and the online Gaussian mixture model

4.1. Complex-valued OGMM algorithm derivation

The objective of the proposed algorithm is to maximize the posterior function in Eq. (11). However, Eq. (11) is difficult to solve for the logarithm of the sum. Thus the Expectation-Maximization (EM) algorithm [39,40] is applied to solve the parameters estimation problem. The algorithm will iterate between calculating responsibilities of all Gaussian components (E Step) and maximizing the parameters $\{\boldsymbol{\Pi}, \boldsymbol{\Sigma}, v, \boldsymbol{U}\}$ (M Step). Assume a latent variable z_{ik}^t in the model, which can be denoted as:

$$z_{ik}^t = \begin{cases} 1, & p_i^t \text{ comes from the } k\text{th Gaussian,} \\ 0, & \text{otherwise.} \end{cases} \tag{15}$$

Hence, the posterior function for complete data will be:

$$[\mathbf{\Pi}, \mathbf{\Sigma}, \boldsymbol{v}, \boldsymbol{U}, \boldsymbol{z}] = [\boldsymbol{p}^t, \boldsymbol{z}^t | \mathbf{\Pi}, \mathbf{\Sigma}, \boldsymbol{v}, \boldsymbol{U}][\mathbf{\Pi}^t | \Theta^{t-1}] \\ [\mathbf{\Sigma}^t | \Theta^{t-1}][\boldsymbol{U}^t | \Theta^{t-1}]. \tag{16}$$

The log-likelihood function for complete data is:

$$\ln([\boldsymbol{p}^t, \boldsymbol{z}^t | \mathbf{\Pi}, \mathbf{\Sigma}, \boldsymbol{v}, \boldsymbol{U}]) = \sum_{k=1}^{K} \left\{ N_k^t \ln(\pi_k^t) \right. \\ \left. + \sum_{i=1}^{d} z_{ik}^t \left(\ln \left\{ \frac{1}{\sigma_k^2 \pi} exp \left(-\frac{|p_i^t - \boldsymbol{u}_i^t \boldsymbol{v}|^2}{\sigma_k^2} \right) \right\} \right) \right\}, \tag{17}$$

where $N_k^t = \sum_{i=1}^{d} z_{ik}^t, k = 1, \ldots, K$, $N^t = \sum_{k=1}^{K} N_k^t$. The likelihood function changed in the log posterior function after introducing of the latent variables, while R_F^t and R_B^t did not change. According to the solution steps of the EM algorithm, the Q function corresponding to Eq. (11) is first defined as follows:

$$Q(\theta, \Theta^{old}) = \mathbb{E}_{\boldsymbol{z}^t} \left(\ln[\boldsymbol{p}^t, \boldsymbol{z}^t | \Theta] | \boldsymbol{p}^t, \Theta^{old} \right) \\ = \mathbb{E}_{\boldsymbol{z}_{ik}^t} \left[\sum_{k=1}^{K} \left\{ N_k^t \ln(\pi_k^t) \right. \right. \\ \left. \left. + \sum_{i=1}^{d} z_{ik}^t \left(-\ln \pi - 2 \ln \sigma_k^t - \frac{|p_i^t - \boldsymbol{u}_i^t \boldsymbol{v}|^2}{\sigma_{k,t}^2} \right) \right\} \right] \\ + R_F^t(\mathbf{\Pi}, \mathbf{\Sigma}) + R_B^t(\boldsymbol{U}). \tag{18}$$

E step aims to estimate the expectation of latent variable z_{ik}^t, $\mathbb{E}[z_{ik}^t]$ needs to be calculated for maximizing the Q function:

$$\mathbb{E}[z_{ik}^t] = 1 \cdot [z_{ik} = 1 | p_i^t, \Theta] + 0 \cdot [z_{ik} = 0 | p_i^t, \Theta] \\ = \frac{[z_{ik} = 1, p_i^t | \Theta]}{[p_i^t | \Theta]} = \frac{[z_{ik} = 1 | \Theta][p_i^t, z_{ik} = 1 | \Theta]}{\sum_{k=1}^{K} [z_{ik} = 1 | \Theta][p_i^t, z_{ik} = 1 | \Theta]} \\ = \frac{\pi_k N_{\mathbb{C}}(p_i^t | \boldsymbol{u}_i^{t^T} \boldsymbol{v}, \sigma_k^2)}{\sum_{k=1}^{K} \pi_k N_{\mathbb{C}}(p_i^t | \boldsymbol{u}_i^{t^T} \boldsymbol{v}, \sigma_k^2)}, \tag{19}$$

where $\pi_k = [z_{ik} = 1 | \Theta]$ means the probability that p_i^t is generated from the distribution of kth Gaussian model. $\mathbb{E}[z_{ik}^t]$ means the observed data p_i^t comes from the kth component of the GMM and is called the responsibility of observed data p_i^t.

Then the M-step can be implemented, it can maximize the Q function after $\mathbb{E}[z_{ik}^t]$ is calculated to approximate z_{ik}^t with the parameters $\{\mathbf{\Pi}, \mathbf{\Sigma}, \boldsymbol{v}, \boldsymbol{U}\}$:

$$\Theta^{new} = \arg\max_{\Theta} Q(\mathbf{\Theta}, \mathbf{\Theta}^{old}). \tag{20}$$

First, the Lagrange method is adopted to update $\mathbf{\Pi}, \mathbf{\Sigma}$. Only $\mathbf{\Pi}, \mathbf{\Sigma}$ is calculated in this step so that it can get the simplified formulation:

$$\mathcal{L}^t(\mathbf{\Pi}, \mathbf{\Sigma}) = -\mathbb{E}_{\boldsymbol{z}^t} \ln([\boldsymbol{p}^t, \boldsymbol{z}^t | \mathbf{\Pi}, \mathbf{\Sigma}, \boldsymbol{v}, \boldsymbol{U}]) + R_F^t(\mathbf{\Pi}, \mathbf{\Sigma}) + R_B^t(\boldsymbol{U}) \\ = \sum_{k=1}^{K} N_k^{t-1} \left(\frac{\sigma_{k,t-1}^2}{2\sigma_{k,t}^2} + \ln \sigma_k \right) - N^{t-1} \sum_{k=1}^{K} \pi_k^{t-1} \ln \pi_k^t \\ - \sum_{i=1}^{d} \sum_{k=1}^{K} z_{ik}^t \left(-\ln \pi - 2 \ln \sigma_k^t - \frac{|p_i^t - \boldsymbol{u}_i^t \boldsymbol{v}|^2}{\sigma_{k,t}^2} \right). \tag{21}$$

The closed-form expressions to update $\mathbf{\Pi}, \mathbf{\Sigma}$ according to (A.3)–(A.6) read:

$$\pi_k^t = \frac{N_k^{t-1} + \sum_{i=1}^{d} z_{ik}^t}{\sum_{k=1}^{K} N_k^{t-1} + \sum_{i=1}^{d} z_{ik}^t}, \tag{22}$$

$$\sigma_{k,t}^2 = \frac{N_k^{t-1} \sigma_{k,t-1}^2 + \sum_{i=1}^{d} z_{ik}^t |p_i^t - \boldsymbol{u}_i^t \boldsymbol{v}|^2}{N_k^{t-1} + \sum_{i=1}^{d} z_{ik}^t}. \tag{23}$$

The iteration rule for $\boldsymbol{v}$ can be obtained by minimizing the term related to $\boldsymbol{v}$ in Eq. (21) and can be expressed as:

$$\min_{\boldsymbol{v}} \| \boldsymbol{w}^t \odot (\boldsymbol{p}^t - \boldsymbol{U}^t \boldsymbol{v}^t) \|_F^2, \tag{24}$$

where $\odot$ denotes the denotes the Hadamard product, each element in $\boldsymbol{w}^t$ is $\boldsymbol{w}_i^t = \sqrt{\sum_{k=1}^{K} \frac{\mathbb{E}[z_{ik}^t]}{2\sigma_{k,t}^2}}, i = 1, \ldots, d$. This is a weighted least square (WLS) problem and has a closed-form solution as

$$\boldsymbol{v}^t = (\boldsymbol{U}^* \boldsymbol{W} \boldsymbol{U}^T)^{-1} \boldsymbol{U}^* \boldsymbol{W} \boldsymbol{p}^t. \tag{25}$$

Finally, the iteration rule of $\boldsymbol{U}$ can be obtained by minimizing Eq. (26):

$$\mathcal{L}^t((U)) = -\mathbb{E}_{\boldsymbol{z}^t} \{ \ln([\boldsymbol{p}^t, \boldsymbol{z}^t | \mathbf{\Pi}, \mathbf{\Sigma}, \boldsymbol{v}, \boldsymbol{U}]) + \ln([\boldsymbol{U} | \mathbf{\Sigma}^{t-1}]) \} \\ = \| \boldsymbol{w}^t \odot (\boldsymbol{p}^t - \boldsymbol{U}^t \boldsymbol{v}^t) \|_F^2 + R_B^t(\boldsymbol{U}). \tag{26}$$

According to (A.7)–(A.9), the solution for each row vector can be formed as:

$$\boldsymbol{u}_i^t = (\rho(\boldsymbol{A}_{i,t-1}^*)^{-1} + w_{i,t}^2 \boldsymbol{v}^* \boldsymbol{v}^T)^{-1} \\ \cdot (w_{i,t}^2 p_i^t \boldsymbol{v}^* + \rho(\boldsymbol{A}_{i,t-1}^*)^{-1} \boldsymbol{u}_i^{t-1}). \tag{27}$$

And if

$$\boldsymbol{A}_{i,t}^* = (\rho(\boldsymbol{A}_{i,t-1}^*)^{-1} + w_{i,t}^2 \boldsymbol{v}^* \boldsymbol{v}^T)^{-1}, \tag{28}$$

$$\boldsymbol{b}_i^t = w_{i,t}^2 p_i^t \boldsymbol{v}^* + \rho(\boldsymbol{A}_{i,t-1}^*)^{-1} \boldsymbol{u}_i^{t-1}, \tag{29}$$

the updating rule for $\boldsymbol{u}_i^t$ can be formed as $\boldsymbol{u}_i^t = \boldsymbol{A}_{i,t}^* \boldsymbol{b}_i^t$. Note that $\boldsymbol{u}_i^{t-1} = \boldsymbol{A}_{i,t-1}^* \boldsymbol{b}_i^{t-1}$, then the update rules for $\boldsymbol{A}_{i,t}^*, \boldsymbol{b}_i^t$ can be formulated from the Binomial Inverse Theory as:

$$\boldsymbol{A}_{i,t}^* = \frac{1}{\rho} \left(\boldsymbol{A}_{i,t-1}^* - \frac{w_{i,t}^2 \boldsymbol{A}_{i,t-1}^* \boldsymbol{v}^* \boldsymbol{v}^T \boldsymbol{A}_{i,t-1}^*}{\rho + w_{i,t}^2 \boldsymbol{v}^T \boldsymbol{A}_{i,t-1}^* \boldsymbol{v}^*} \right), \tag{30}$$

$$\boldsymbol{b}_i^t = w_{i,t}^2 p_i^t \boldsymbol{v}^* + \rho \boldsymbol{b}_i^{t-1}. \tag{31}$$

4.2. Complex-valued OGMM algorithm chart and complexity analysis

The solving process of the proposed method is shown in Algorithm 1. For the data in the new frame with N sampling

---

Algorithm 1 Complex-valued OGMM algorithm.

1: Initialization: the parameters $\mathbf{\Pi}^{t-1}, \mathbf{\Sigma}^{t-1}, N^{t-1}, \boldsymbol{A}_i^{t-1}, \boldsymbol{b}_i^{t-1} \boldsymbol{v}^t$, iteration number $n_{iter}, n_{tmp} = 0$
2: **if** $n_{tmp} < n_{iter}$ **then**
3: $\quad n_{tmp} = n_{tmp} + 1$
4: $\quad$ Update z_{ik}^t based on Eq. (19) $\mathbb{E}[z_{ik}^t] = \frac{\pi_k N_{\mathbb{C}}(p_i^t | \boldsymbol{u}_i^{t^T} \boldsymbol{v}, \sigma_k^2)}{\sum_{k=1}^{K} \pi_k N_{\mathbb{C}}(p_i^t | \boldsymbol{u}_i^{t^T} \boldsymbol{v}, \sigma_k^2)}$
5: $\quad$ Update $\{\mathbf{\Pi}^{t-1}, \mathbf{\Sigma}^{t-1}, N^{t-1}\}$ based on Eqs. (22) and (23) $\pi_k^t = \frac{N_k^{t-1} + \sum_{i=1}^{d} z_{ik}^t}{\sum_{k=1}^{K} N_k^{t-1} + \sum_{i=1}^{d} z_{ik}^t} \sigma_{k,t}^2 = \frac{N_k^{t-1} \sigma_{k,t-1}^2 + \sum_{i=1}^{d} z_{ik}^t |p_i^t - \boldsymbol{u}_i^t \boldsymbol{v}|^2}{N_k^{t-1} + \sum_{i=1}^{d} z_{ik}^t}$
6: $\quad$ Update $\boldsymbol{v}^t$ based on Eq. (25) $\boldsymbol{v}^t = (\boldsymbol{U}^* \boldsymbol{W} \boldsymbol{U}^T)^{-1} \boldsymbol{U}^* \boldsymbol{W} \boldsymbol{p}^t$.
7: **end if**
8: **if** $i <= d$ **then**
9: $\quad$ update $\{\boldsymbol{A}_{i,t}^*\}_{i=1}^d, \{\boldsymbol{b}_i^t\}_{i=1}^d$ based on Eqs. (30) and (31) $\boldsymbol{A}_{i,t}^* = \frac{1}{\rho}(\boldsymbol{A}_{i,t-1}^* - \frac{w_{i,t}^2 \boldsymbol{A}_{i,t-1}^* \boldsymbol{v}^* \boldsymbol{v}^T \boldsymbol{A}_{i,t-1}^*}{\rho + w_{i,t}^2 \boldsymbol{v}^T \boldsymbol{A}_{i,t-1}^* \boldsymbol{v}^*}) \boldsymbol{b}_i^t = w_{i,t}^2 p_i^t \boldsymbol{v}^* + \rho \boldsymbol{b}_i^{t-1}$
10: $\quad$ update $\boldsymbol{u}_i^t = \boldsymbol{A}_{i,t}^* \boldsymbol{b}_i^t$
11: **end if**
Ensure: $\mathbf{\Pi}^t, \mathbf{\Sigma}^t, N^t, \boldsymbol{v}^t, \boldsymbol{U}^t, \{\boldsymbol{A}_{i,t}^*\}_{i=1}^d, \{\boldsymbol{b}_i^t\}_{i=1}^d$

---

points, the computational complexity of the STFT is $O(N \log_2 N)$, and the complexity of the EM algorithm is $O(KN)$ [41]. It can be

considered that the complexity related to the rank is $O(1)$ since the rank is much smaller than the data dimension N. The complexity of the proposed algorithm is $O(N^2)$ when the matrix multiplication is taken into account. The computational complexity will be improved since the calculation is performed in the complex number domain.

The specific initialization process of the algorithm is as follows. First, 20 frames of data are selected, and the PCA algorithm is used to perform simple initialization to obtain U and v. The initialization of A and b is performed by using Eqs. (28) and (29). N^{t-1} is a fixed value and is set to $5d$ or $10d.\rho$ is set to 0.99. As for the parameters of the GMM, the weight can be uniformly set to $1/k$, the mean is initialized to 0, and the variance is initialized to 1 for each Gaussian model. The elements in the parameter matrix w can be initialized to 1/d. Then it can be iterated according to the process in Algorithm 1.

5. Simulations and experiment data validation

5.1. Simulation of the synthetic data

In this section, the numerical simulations are operated with the MATLAB R2019b software on Intel(R) Core (TM) i7-8750H @ 2.20 GHz, GTX 1060 system with 8 GB RAM to evaluate the performance of the OGMM algorithm. The simulation steps are as follows: firstly, the original harmonic signal is generated; then, the complex noise is added to the original signal; finally, the algorithms are adopted to denoise the contaminated signal. The signal after denoising is compared with the original signal to verify the performance of the algorithm. The expressions of harmonic signals are listed below:

- **Signal 1**: $y_1(t) = (1 + 0.5\sin(500t)) \cdot \cos(800t)$,
- **Signal 2**: $y_2(t) = 0.5\sin(120t) + \sin(360t - 1.2) + 0.7\sin(600t - 1.6) + \sin(1800t + 0.5)$.

Signal 1 is sampled at 500 Hz for 380 s and **Signal 2** is sampled at 4000 Hz for 35 s.

Then the non-stationary noise is added to the original signal. The method for constructing non-stationary noise is described: the original signal is divided into 100 frames. Then, the non-Gaussian and non-stationary noise is added within each frame. The images of the noise-free signal and the noisy signal are shown in Fig. 4.

The complex noise in each frame consists of three Gaussian components:

- **Noise 1**: the first Gaussian noise has a variance of 0.01, and the mean follows a uniform distribution $U(0, 2)$, the second Gaussian noise has a variance of 0.01, and the mean follows a uniform distribution $U(-2, 0)$, and the last Gaussian noise has a mean of 0, and the variance follows a uniform distribution $U(0, 1)$. The PDF of the non-stationary complex noises in the first five frames is shown in Fig. 5(a). The SNR of the whole time series is 1.02 dB,
- **Noise 2**: the first Gaussian noise has a variance of 1.44, and the mean follows a uniform distribution $U(-1, 0)$, the second Gaussian noise has a variance of 1.44, and the mean follows a uniform distribution $U(0, 2)$, and the last Gaussian noise has a mean of 0, and the variance follows a uniform distribution $U(0, 1)$. The PDF of the non-stationary complex noises in the first five frames is shown in Fig. 5(b). The SNR of the whole time series is -0.61 dB.

The OGMM algorithm is mainly verified by comparing with the Hankel SVD (HSVD) [24], the Particle Filtering (PF) [42], and the Block Thresholding Wavelet(BTW) algorithms[43]. The PF is efficient at dealing with nonlinear non-Gaussian problems. Higher-order statistics are used in the BTW algorithm, and the parame-
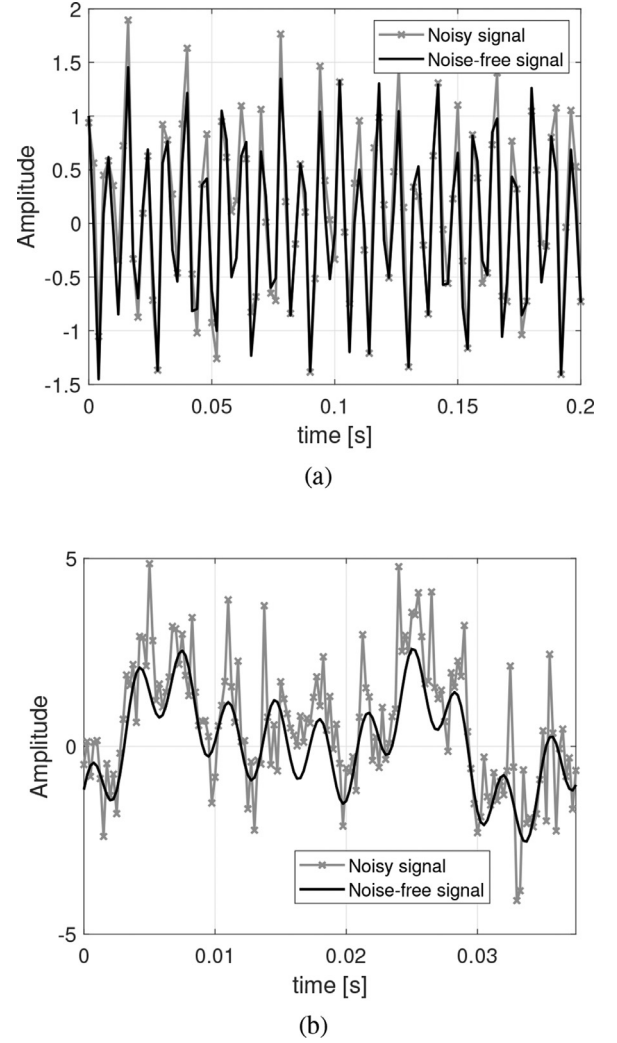

(a)

(b)

Fig. 4. The noise-free signal and the noisy signal in (a) **Signal 1** with **Noise 1**, (b) **Signal 2** with **Noise 2**.

ters for BTW are adaptively adjusted to the inferred signal property. The relative error is defined for evaluating the algorithm:

$$\delta = \frac{\|\chi - \hat{\chi}\|_{\text{norm}}^2}{\|\chi\|_{\text{norm}}^2}, \tag{32}$$

where χ can denote time signal, STFT matrix, or the estimated frequency, $\hat{\chi}$ is the estimation of χ. When χ is a vector, the norm corresponds to the ℓ_2 norm, and when χ is a matrix, the norm is the Frobenius norm.

In this part, the OGMM algorithm is executed in the time-frequency domain, and the denoised time-frequency matrix is transformed into the time domain by ISTFT. The relative errors of the time-frequency matrix before and after denoising are shown in Fig. 6. The relative error of the contaminated matrix is large and fluctuates sharply, reflecting the non-stationary characteristic of the noise. However, the relative error after denoising is small and tends to be stationary, reflecting the OGMM algorithm's effectiveness for denoising in the time-frequency domain and the fitting performance of the GMM for non-stationary noise. The mean value of the relative error from frame 50 to frame 100 before denoising is 0.96, and the variance is 0.0596, but after denoising, it is reduced to 0.26 and 0.0019 for **Signal 1**, respectively.

The relative errors of the time domain results for 100 frames are shown in Fig. 7. The result of denoising by HSVD and BTW is
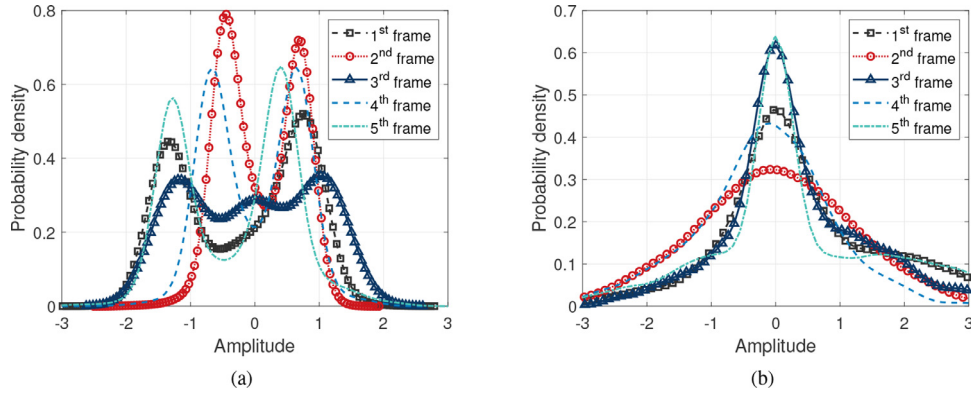
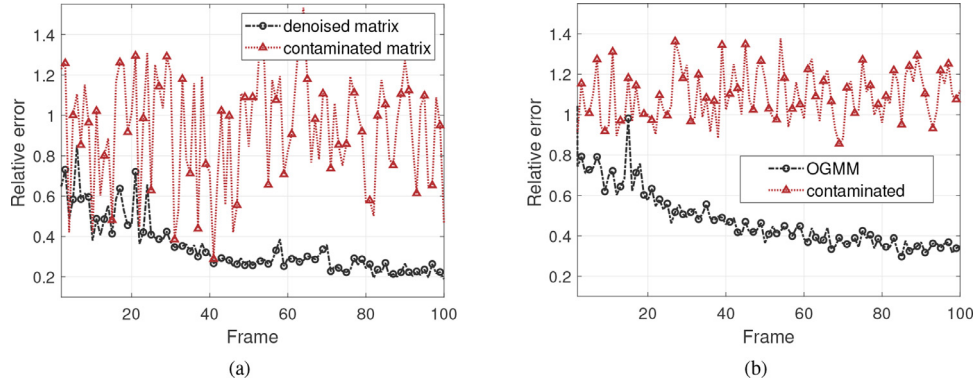**Fig. 5.** The PDF of the first 5 frames in (a) **Noise 1**, (b) **Noise 2**.

Fig. 6. The relative error of the STFT matrix within 100 frames of (a) **Signal 1** with **Noise 1**, (b) **Signal 2** with **Noise 2**.
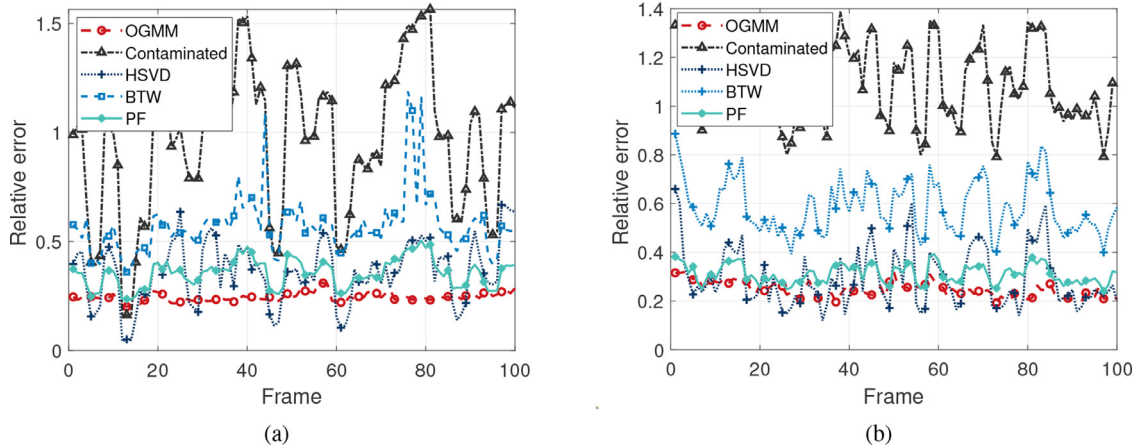

Fig. 7. The relative error of the time domain signal within 100 frames of (a) **Signal 1** with **Noise 1**, (b) **Signal 2** with **Noise 2**.

not stable enough though the relative errors on some frames are smaller than those of the OGMM algorithm. The performance of the offline algorithm depends greatly on the statistical properties of the noise, while the OGMM algorithm has a more stable denoising performance. The mean relative error of the time sequence is 0.36 with a variance of 0.02 for HSVD, 0.35 with a variance of 0.0042 for PF, and 0.57 with a variance of 0.02 for BTW. It is reduced to 0.24 with a variance of 0.0004 using OGMM for **Signal 1**. The mean relative error of the time sequence for **Signal 2** is 0.24 with a variance of 0.001 for OGMM and 0.31 with a variance of 0.0015 for PF.

From the relative error of the time-domain denoising results, the relative error of the OGMM algorithm is the smallest and the most stable between frames. The denoising effect of the PF algorithm is the closest to the OGMM, but the signal needs to be mod-

eled in the state space before using the PF algorithm. The algorithm proposed in this paper only needs to perform STFT, which is much more convenient in application.

The computational speed of the proposed algorithm is related to the input data size and algorithm parameters, including the length of the window, the number of signal sampling points, the number of EM algorithm iterations, etc. In this simulation, the number of EM algorithm iterations is set to 50, and the dimensionality of each STFT matrix frame is about 256 by 250. The total time required to process 100 frames of **Signal 1** was 230 s, and that of **Signal 2** was 150 s. For Signal 1, the processing speed is 2.3 s per frame, and each frame contains 1900 samples. The processing speed of the algorithm depends on the amount of data per frame. The practicality of the proposed algorithm, in reality, depends on the real-time update and refresh rate requirements of the appli-
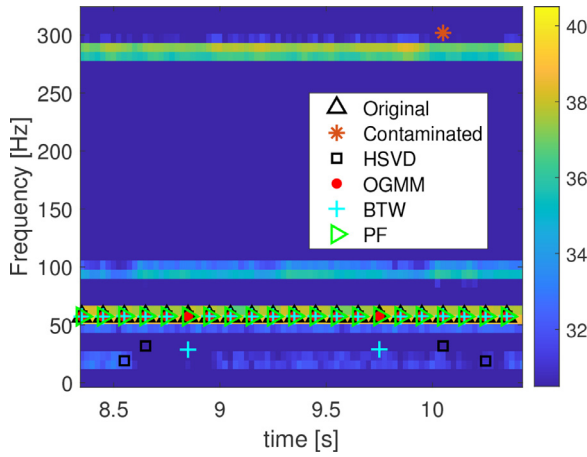
Fig. 8. The foundamental frequency estimation results of **Signal 2** with **Noise 2**.

Fig. 9. The box plot of the time sequence relative error using the contaminated signal. The OGMM denoising signal(with different rank settings), the HSVD denoising signal, the BTW denoising signal, and the PF denoising signal. The relative error within 100 frames of **Signal 1** with **Noise 1** is shown in (a), **Signal 2** with **Noise 2** is shown in (b).

cation scenario. For example, it is more important to extract the feature frequencies for helicopter rotor signals, while the requirements for acquiring their real-time changes are not very stringent. The processing time of **Signal 2** is reduced to 82 s and still maintains good results if the dimensionality of the STFT matrix is reduced to 256 by 100 by changing the overlap length. When the dimension of the matrix is reduced to 256 by 50, its calculation time decreases but the average relative error increases to 0.51. The denoising effect is unsatisfactory if the frame is too small, and the frame length selection should be considered comprehensively. According to the experience of numerical simulation, the dimension of each frame matrix is set to about 256 by 200, which can meet the requirements of time-consuming and performance. The most time-consuming part of the algorithm is the EM algorithm iteration. The Gaussian component number in the GMM is set to 3, and the iterations is set to 100 to meet most requirements.

To further verify the denoising effect of the OGMM algorithm, the time sequence after denoising is used as the input of the fast Non-linear Least Square (Fast-NLS) algorithm, which can quickly and accurately estimate the fundamental frequency components of the time series [44]. The fundamental frequency estimation results of the original signal, the contaminated signal, and the denoised signal are shown in Fig. 8. It can be seen from Fig. 8 that the fundamental frequency of the signal can be estimated, which is consistent with the fundamental frequency of **Signal 2**. And the fundamental frequency can not be detected using the noisy signal at a lower SNR. The average relative errors of the fundamental frequency estimation using HSVD, OGMM, BTW, and PF denoising were 0.13,0.11,0.06, and 0.01, respectively, and the numbers of no errors among 128 estimation points were 57, 90, 47, and 85, respectively.

To further explore the effect of parameters on the OGMM algorithm, the assumptions on the rank of the low-rank matrices are changed to obtain different relative error results in the time domain. The rank of the matrix is set to 2 to 16 for the OGMM algorithm, and the box plot of the denoising results is shown in Fig. 9. The box plot can clearly and directly express the basic statistical characteristics of the relative errors within 100 frames. The dashed line of the HSVD results is longer than that of the OGMM results in Fig. 9, which means that the variance of the former is larger. The relative error distribution of OGMM is more concentrated than the results of HSVD, BTW, and PF. It can be found that for **Signal 1**, the denoising results deteriorate sharply when $r = 2$ and do not change much when $r \geq 4$. As for **Signal 2**, the relative error is better when $r \geq 8$. It can be concluded that the results deteriorate when the low-rank matrix is underestimated, while it is not influenced when overestimated. Therefore, the rank of the matrix can
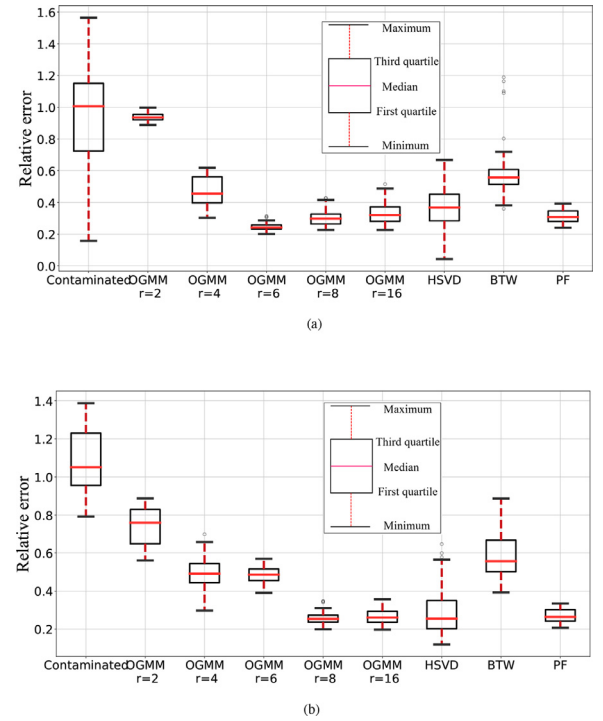
Table 1
Relative errors after denoising with OGMM under different harmonic parameters.

	Value	Mean	Variance
Amplitude	0.001	0.4529	0.0122
	0.01	0.4147	0.0099
	0.1	0.3081	0.0032
	1	0.2817	7.77E-04
	10	0.2776	4.20E-04
	100	0.2569	3.60E-04
Phase	0.4π	0.2619	4.30E-04
	0.8π	0.2638	3.90E-04
	1.2π	0.2548	3.40E-04
	1.6π	0.2576	2.60E-04
	2π	0.2738	6.80E-04
Frequency	1	0.2043	6.10E-04
	10	0.1906	2.50E-04
	100	0.2435	3.60E-04
	1000	0.3754	2.60E-04

be set to twice the number of harmonics or little higher in practice, which will not have undesirable results except for increasing calculation consumption.

To further determine the application boundary of the OGMM algorithm, the phase, amplitude, and frequency of the harmonic signal are changed to simulate. The simulation is carried out for only one sinusoidal signal, the overall SNR of the simulated signal is 0 dB, and the frequency is fixed to 200 Hz when studying the effect of amplitude and phase. The relative error after denoising with OGMM is shown in Table 1. The model assumptions of the proposed OGMM algorithm are not affected by the magnitude of the signal theoretically, but there may be minor differences in numerical simulations. The possible reason is that a small offset is added at the inversion operations to ensure the stability of the algorithm, and the calculation result may also be influenced by the numerical precision settings of the simulation environment. The phase of the harmonic signal has little effect on the denoising effect, and
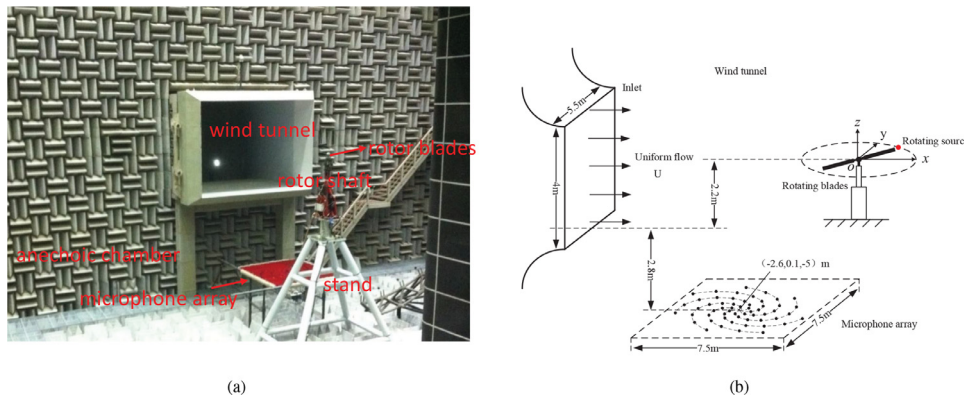
Fig. 10. Rotor blades tests in a wind tunnel. (a) The layout of the experiment; (b) The schematic diagram.

the relative error after denoising is about 0.27. It can be seen from Table 1 that the frequency seems to have an effect on the denoising results. In theory, the assumption of the low-rank model is not changed by the frequency. In these simulations, the effect of frequency on denoising performance comes from the sampling frequency setting. For the OGMM algorithm, a higher sampling frequency can get better results. For the 1000 Hz signal in the table, when the sampling rate is 10 kHz, its relative error is 0.3754, and when the sampling rate is 20 kHz, its relative error is reduced to 0.2656. Oversampling increases the information content and makes it better to learn the unchanged harmonics between frame and frame iterations.

5.2. Wind tunnel experiment data validation

In order to verify the effectiveness of the algorithm for real-world data processing, rotor acoustic harmonic signals with non-Gaussian and non-stationary noises from acoustic wind tunnel tests are used in this section. A high level of aerodynamic signal is generated when the rotor blades are operating, which is a major part of the helicopter noise. The main component of rotor aerodynamic noise is rotating noise. Rotating noise is the periodic sound pressure disturbance produced by the periodic pulsating force acting on the blade and the thickness of the blade. The main characteristic of rotating noise is that its frequency spectrum is composed of various harmonics of the blade passing frequency. Due to the high air velocity in the wind tunnel test, the interference sources include wind noise, rotor support tower noise, etc., resulting in non-stationary complex broadband background noise. Since the noise is broadband noise and there are multiple harmonic components, it is difficult to use a simple low-pass filter to meet the application requirements. The schematic diagram of the experiment is shown in Fig. 10 [45]. For the experiment, the rotor's blade passing frequency fluctuates around 6 Hz considering the slight rotational speed fluctuations. Microphone measurements are taken at a sampling frequency of 51.2 kHz within 30 s of data collected in 139 microphone channels.

In this paper, the sound pressure signal of channel 32 is denoised using the OGMM algorithm and a Chebyshev lowpass filter with a cutoff frequency of 30 Hz. The signal length is 170000, the signal is divided into 100 frames, and there are 504 data overlaps between every two frames. In each frame, a Hamming window with a length of 512 is used for STFT, and the matrix size of each frame is 257 by 211. The Gaussian component number is set to 3, and the parameters of each Gaussian model are randomly initialized. The original sound pressure collected by one of the microphones, the sound pressure after denoising using OGMM, and the lowpass filter are shown in Fig. 11. The signal denoised by the lowpass filter is smoother but has a phase deviation from the orig-
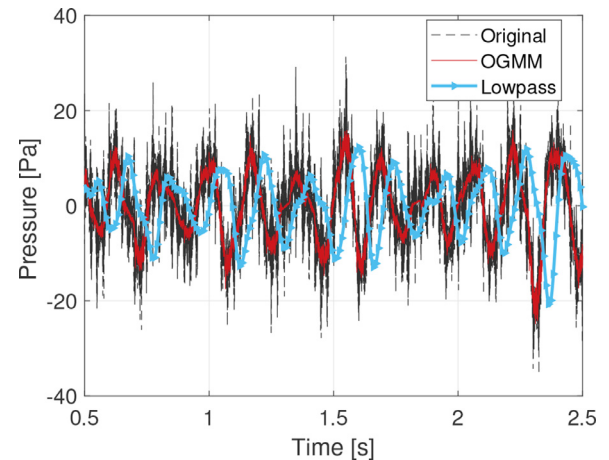

Fig. 11. The time-domain results of the experimental data. The experimental data comes from channel 32 and is taken at a sampling frequency of 51.2 kHz within 30 s. The cutoff frequency of the Chebyshev lowpass filter is 30 Hz. As for the OGMM algorithm, the signal is divided into 100 frames, the length of the Hamming window is 512, and there are 504 data overlaps between every two frames. The matrix size of each frame is 257 by 211. The Gaussian component number is set to 3.

inal signal. The raw test signal with significant modulation is corrupted with strong noises due to the flow-induced shaft and the stand noise. The FFT results and the power spectral density diagram of the original signal, the OGMM denoised signal, and the lowpass filter denoised signal are shown in Fig. 12(a) and (b), respectively. The amplitude of FFT of the signal denoised by OGMM is closer to that of the original signal. And the frequency components other than the blade passing frequency of 6.25 Hz are greatly reduced in Fig. 12. Although the lowpass filter seems to be able to achieve good results from the experimental data processing results, the lack of practicability of the lowpass filter and the advantages of the proposed algorithm can still be found in two aspects. The first is that the broadband noise will affect the quality of acoustic imaging. The lowpass filter can indeed extract the harmonic signal, but it will also introduce noise in the frequency range of the lowpass filter. For rotating instruments, the characteristic frequency includes the rotational frequency and the product of the rotational frequency, and the number of blades. The lowpass filter can extract a certain order harmonic but remove other frequency components, such as 62.5 Hz. Secondly, the passing frequency of the blades in practical helicopter detection is often unavailable, which is required as the prior knowledge to design an appropriate lowpass filter. The proposed method can extract harmonics without prior conditions, which is a major advantage. The OGMM algorithm has the advantage that it does not require prior information, and

(a)

(b)
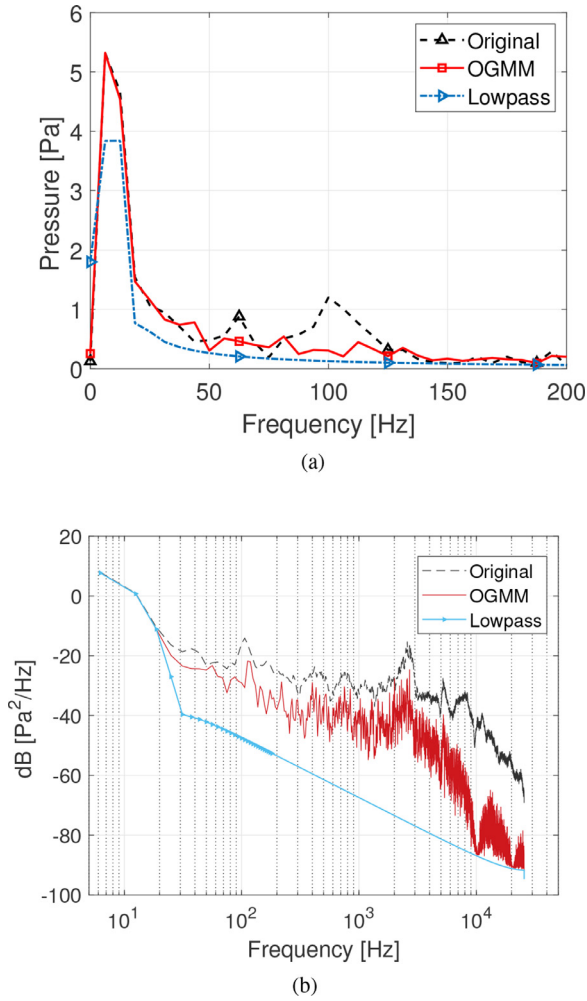
Fig. 12. (a) The FFT results in frequency range from 0Hz to 200Hz. The amplitude of FFT of the signal denoised by OGMM is closer to that of the original signal. (b)The power spectral density diagram of the experimental data obtained by the pwelch method with a window width of 8192 and an overlap length of 4096.

the design of a lowpass filter to denoise the signal needs to know the specific frequency in advance.

6. Conclusion

Many noise reduction methods have been applied as pre-processing for extracting signal features, such as fundamental frequency estimation. In past studies, the noise distribution was usually assumed to be Gaussian and stationary, while in reality, the noise distribution is more complicated. A denoising method based on online-GMM and low-rank subspace decomposition under the MAP framework is proposed in this paper, and the simulation verifies its superior denoising performance. Some developments have been made in harmonic denoising for non-stationary and non-Gaussian noise, which can be applied in most harmonic signal scenarios since no assumptions are made on the harmonic signal. The proposed algorithm in this paper is updated in an online way, and the real-time applications will be further developed in the future.

Declaration of Competing Interest

The authors declare that they have no known competing financial interests or personal relationships that could have appeared to influence the work reported in this paper.

Appendix A. Derivation for the prior parameter settings and the online EM algorirhm

The method of setting the prior parameters and the detailed derivation of the EM algorithm will be shown in Appendix A. To set the conjugate prior of the tth frame, consider the complete data likelihood function of the previous $t-1$ frame

$$\sum_{j=1}^{t-1}[\boldsymbol{p}^j, \boldsymbol{z}^j | \boldsymbol{\Pi}, \boldsymbol{\Sigma}, \boldsymbol{\nu}^j, \boldsymbol{U}^j] = \sum_{j=1}^{t-1}\sum_{i=1}^{d}\sum_{k=1}^{K} z_{ik}^j$$

$$\{\ln \pi_k^j + \ln N_{\mathbb{C}}(\boldsymbol{u}_i^{jT}\boldsymbol{\nu}^j, \sigma_k^{2j})\}$$

$$= \sum_{j=1}^{t-1}\sum_{i=1}^{d}\sum_{k=1}^{K} z_{ik}^j \left\{\ln \pi_k^j + \left(-2\ln\sigma_k^t - \frac{|p_i^t - \boldsymbol{u}_i^t \boldsymbol{\nu}|^2}{\sigma_{k,t}^2}\right)\right\}$$

$$= \sum_{k=1}^{K}\left\{\sum_{j=1}^{t-1}\sum_{i=1}^{d}\left\{z_{ik}^j \ln\pi_k^j - 2z_{ik}^j \ln\sigma_k^j - \frac{z_{ik}^j |p_i^j - \boldsymbol{u}_i^j \boldsymbol{\nu}^j|^2}{\sigma_k^{j2}}\right\}\right\}. \quad \text{(A.1)}$$

Let $\sum_{j=1}^{t-1}\sum_{i=1}^{d} z_{ik}^j = N_k^{t-1}$, which represents the amount of data from the kth Gaussian model in the previous $t-1$ frame. Let $\pi_k^{t-1} = \frac{N_k^{t-1}}{N^{t-1}}$, and π_k^{t-1} means the responsibility of the kth model. Let $\frac{\sum_{j=1}^{t-1}\sum_{i=1}^{d} z_{ik}^j |p_i^j - \boldsymbol{u}_i^j \boldsymbol{\nu}^j|^2}{N_k^{t-1}} = \sigma_{k,t-1}^2$. Then the formulation can be written as:

$$\sum_{k=1}^{K}\left(N_k^{t-1}\ln(\pi_k^t) - 2N_k^{t-1}\ln\sigma_k^t - \sigma_{k,t-1}^2 \frac{N_k^{t-1}}{\sigma_{k,t}^2}\right)$$

$$= N_k^{t-1}\sum_{k=1}^{K}\pi_k^{t-1}\ln(\pi_k^t) - \sum_{k=1}^{K}N_k^{t-1}\left(2\ln\sigma_k^t + \frac{\sigma_{k,t-1}^2}{\sigma_{k,t}^2}\right). \quad \text{(A.2)}$$

Compare the standard Dirichlet distribution $\boldsymbol{\Pi} \sim \text{Dir}(\boldsymbol{\alpha}) = C \cdot \prod_{k=1}^{K}\pi_k^{\alpha_k - 1}$ with the formulation, then $\alpha_k = N_k^{t-1}\pi_k^{t-1} + 1$. Compare the standard Inv-Gamma distribution $\sigma_k^2 \sim \text{Inv} - \text{Gamma}(\alpha, \lambda) = C \cdot \lambda^\alpha (\sigma_k^2)^{\alpha-1}\exp(-\frac{\lambda}{\sigma_k^2})$ with the formulation, then $\alpha = N_k^{t-1} - 1, \lambda = N_k^{t-1}\sigma_{k,t-1}^2$.

The Langrangian method is used to obtain the solution of $\boldsymbol{\Pi}$ and $\boldsymbol{\Sigma}$.

$$\frac{\partial \mathcal{L}^t(\boldsymbol{\Pi}, \boldsymbol{\Sigma})}{\partial \sigma_k} = \sum_{i=1}^{d} z_{ik}^t \left\{\frac{1}{\sigma_k} - \frac{|p_i^t - \boldsymbol{u}_i^t \boldsymbol{\nu}|^2}{\sigma_k^3} + N_k^{t-1}\left(\frac{\sigma_{k,t-1}^2 + \sigma_k^2}{\sigma_k^3}\right)\right\}. \quad \text{(A.3)}$$

Let $\frac{\partial \mathcal{L}^t(\boldsymbol{\Pi}, \boldsymbol{\Sigma})}{\partial \sigma_k} = 0$, then the solution can be obtained:

$$\sigma_{k,t}^2 = \frac{N_k^{t-1}\sigma_{k,t-1}^2 + \sum_{i=1}^{d} z_{ik}^t |p_i^t - \boldsymbol{u}_i^t \boldsymbol{\nu}|^2}{N_k^{t-1} + \sum_{i=1}^{d} z_{ik}^t}. \quad \text{(A.4)}$$

Take $\sum_{k=1}^{K}\pi_k = 1$ as the constraint condition to obtain

$$\frac{\partial \mathcal{L}^t((\boldsymbol{\Pi}, \boldsymbol{\Sigma}) + \lambda(\sum_{k=1}^{K}\pi_k - 1))}{\partial \pi_k} = -\sum_{i=1}^{d} z_{ik}^t \frac{1}{\pi_k} - N_k^{t-1}\frac{1}{\pi_k} - \lambda = 0. \quad \text{(A.5)}$$

By summing up k and using $\sum_{k=1}^{K}\pi_k = 1$, then

$$\pi_k^t = \frac{N_k^{t-1} + \sum_{i=1}^{d} z_{ik}^t}{\sum_{k=1}^{K} N_k^{t-1} + \sum_{i=1}^{d} z_{ik}^t}. \quad \text{(A.6)}$$

As for the objective function of $\boldsymbol{U}$, it is equivalent to

$$\mathcal{L}^t((U)) = \sum_{i=1}^{d} w_{i,t}^2 \cdot (p_i^t - \boldsymbol{u}_i^t \boldsymbol{v}) \cdot (p_i^t - \boldsymbol{u}_i^t \boldsymbol{v})^*$$
$$+ \rho \sum_{i=1}^{d} (\boldsymbol{u}_i - \boldsymbol{u}_i^{t-1})^H (\boldsymbol{A}_i^{t-1})^{-1}(\boldsymbol{u}_i - \boldsymbol{u}_i^{t-1}), \qquad (A.7)$$

$$\frac{\partial \mathcal{L}^t(\boldsymbol{U})}{\partial \boldsymbol{u}_i} = w_{i,t}^2(p_i^t - \boldsymbol{u}_i^t \boldsymbol{v})(-\boldsymbol{v}^T) + \rho(\boldsymbol{u}_i - \boldsymbol{u}_i^{t-1})^H(\boldsymbol{A}_i^{t-1})^{-1} = 0, \qquad (A.8)$$

$$\boldsymbol{u}_i^t = (\rho(\boldsymbol{A}_{i,t-1}^*)^{-1} + w_{i,t}^2 \boldsymbol{v}^* \boldsymbol{v}^T)^{-1}$$
$$\cdot (w_{i,t}^2 p_i^t \boldsymbol{v}^* + \rho(\boldsymbol{A}_{i,t-1}^*)^{-1} \boldsymbol{u}_i^{t-1}). \qquad (A.9)$$

References

[1] S.N. Chegini, A. Bagheri, F. Najafi, Application of a new EWT-based denoising technique in bearing fault diagnosis, Measurement 144 (2019) 275–297, doi:10.1016/j.measurement.2019.05.049.

[2] Z. Wang, Q. Zhang, J. Xiong, M. Xiao, G. Sun, J. He, Fault diagnosis of a rolling bearing using wavelet packet denoising and random forests, IEEE Sens. J. 17 (17) (2017) 5581–5588, doi:10.1109/JSEN.2017.2726011.

[3] T.R. Damarla, D. Ufford, Helicopter detection using harmonics and seismic-acoustic coupling, in: E.M. Carapezza (Ed.), Unattended Ground, Sea, and Air Sensor Technologies and Applications X, Society of Photo-Optical Instrumentation Engineers (SPIE) Conference Series, vol. 6963, 2008, p. 69630W, doi:10.1117/12.776899.

[4] S. Akhtar, M. Elshafei-Ahmed, M.S. Ahmed, Detection of helicopters using neural nets, IEEE Trans. Instrum. Meas. 50 (3) (2001) 749–756.

[5] F. Mustire, M. Bouchard, M. Boli, Low-cost modifications of Rao-Blackwellized particle filters for improved speech denoising, Signal Process. 88 (11) (2008) 2678–2692, doi:10.1016/j.sigpro.2008.05.006.

[6] D. Rethage, J. Pons, X. Serra, A wavenet for speech denoising, in: 2018 IEEE International Conference on Acoustics, Speech and Signal Processing (ICASSP), 2018, pp. 5069–5073, doi:10.1109/ICASSP.2018.8462417.

[7] L. Chergui, S. Bouguezel, A new pre-whitening transform domain LMS algorithm and its application to speech denoising, Signal Process. 130 (2017) 118–128, doi:10.1016/j.sigpro.2016.06.021.

[8] J. Yan, L. Lu, Improved Hilbert Huang transform based weak signal detection methodology and its application in incipient fault diagnosis and ECG signal analysis, Signal Process. 98 (2014) 74–87, doi:10.1016/j.sigpro.2013.11.012.

[9] AaYatay Candan, U. Aelebi, Frequency estimation of a single real-valued sinusoid: an invariant function approach, Signal Process. 185 (2021) 108098, doi:10.1016/j.sigpro.2021.108098.

[10] K. Chan, H. So, Accurate frequency estimation for real harmonic sinusoids, IEEE Signal Process. Lett. 11 (7) (2004) 609–612, doi:10.1109/LSP.2004.830115.

[11] E. Wan, R. Van Der Merwe, The unscented Kalman filter for nonlinear estimation, in: Proceedings of the IEEE 2000 Adaptive Systems for Signal Processing, Communications, and Control Symposium (Cat. No.00EX373), 2000, pp. 153–158, doi:10.1109/ASSPCC.2000.882463.

[12] R. Coelho, D. Alves, Real-time lock-in amplifier implementation using a Kalman filter for quasi-periodic signal processing in fusion plasma diagnostics, IEEE Trans. Plasma Sci. 37 (1) (2009) 164–170, doi:10.1109/TPS.2008.2006976.

[13] E. Navon, B. Bobrovsky, An efficient outlier rejection technique for Kalman filters, Signal Process. 188 (2021) 108164, doi:10.1016/j.sigpro.2021.108164.

[14] N.S. Haider, Respiratory sound denoising using empirical mode decomposition, hurst analysis and spectral subtraction, Biomed. Signal Process. Control 64 (2021) 102313, doi:10.1016/j.bspc.2020.102313.

[15] K. Hu, D. Wang, Unvoiced speech segregation from nonspeech interference via CASA and spectral subtraction, IEEE Trans. Audio Speech Lang. Process. 19 (6) (2011) 1600–1609, doi:10.1109/TASL.2010.2093893.

[16] F.M. Bayer, A.J. Kozakevicius, R.J. Cintra, An iterative wavelet threshold for signal denoising, Signal Process. 162 (2019) 10–20, doi:10.1016/j.sigpro.2019.04.005.

[17] Q. Pan, L. Zhang, G. Dai, H. Zhang, Two denoising methods by wavelet transform, IEEE Trans. Signal Process. 47 (12) (1999) 3401–3406, doi:10.1109/78.806084.

[18] A. Baussard, F. Nicolier, F. Truchetet, Rational multiresolution analysis and fast wavelet transform: application to wavelet shrinkage denoising, Signal Process. 84 (10) (2004) 1735–1747, doi:10.1016/j.sigpro.2004.06.001.

[19] H. Jiang, J. Chen, G. Dong, T. Liu, G. Chen, Study on Hankel matrix-based SVD and its application in rolling element bearing fault diagnosis, Mech. Syst. Signal Process. 52–53 (2015) 338–359, doi:10.1016/j.ymssp.2014.07.019.

[20] X. Zhao, B. Ye, Similarity of signal processing effect between Hankel matrix-based SVD and wavelet transform and its mechanism analysis, Mech. Syst. Signal Process. 23 (4) (2009) 1062–1075, doi:10.1016/j.ymssp.2008.09.009.

[21] M.J. Korenberg, A robust orthogonal algorithm for system identification and time-series analysis, Biol. Cybern. 60 (4) (1989) 267–276, doi:10.1007/BF00204124.

[22] R. Bitmead, A. Tsoi, P. Parker, A Kalman filtering approach to short-time Fourier analysis, IEEE Trans. Acoust. 34 (6) (1986) 1493–1501, doi:10.1109/TASSP.1986.1164991.

[23] K.N. Plataniotis, D. Androutsos, A.N. Venetsanopoulos, Nonlinear filtering of non-Gaussian noise, J. Intell. Rob. Syst. 19 (2) (1997) 207–231, doi:10.1023/A:1007974400149.

[24] Y. Yang, J. Rao, Robust and efficient harmonics denoising in large dataset based on random SVD and soft thresholding, IEEE Access 7 (2019) 77607–77617, doi:10.1109/ACCESS.2019.2921579.

[25] M. Zhao, X. Jia, A novel strategy for signal denoising using reweighted SVD and its applications to weak fault feature enhancement of rotating machinery, Mech. Syst. Signal Process. 94 (2017) 129–147, doi:10.1016/j.ymssp.2017.02.036.

[26] M. Fatemi, H. Amindavar, J.A. Ritcey, Noise reduction via harmonic estimation in Gaussian and non-Gaussian environments, Signal Process. 90 (5) (2010) 1554–1561, doi:10.1016/j.sigpro.2009.11.002.

[27] I. Bilik, J. Tabrikian, Mmse-based filtering in presence of non-Gaussian system and measurement noise, IEEE Trans. Aerosp. Electron. Syst. 46 (3) (2010) 1153–1170, doi:10.1109/TAES.2010.5545180.

[28] R. Izanloo, S.A. Fakoorian, H.S. Yazdi, D. Simon, Kalman filtering based on the maximum correntropy criterion in the presence of non-Gaussian noise, in: 2016 Annual Conference on Information Science and Systems (CISS), 2016, pp. 500–505, doi:10.1109/CISS.2016.7460553.

[29] W. Shao, J. Barras, P. Kosmas, A novel wavelets method for cancelling time-varying interference in NQR signal detection, Signal Process. 154 (2019) 238–249, doi:10.1016/j.sigpro.2018.08.016.

[30] R. Sameni, Online filtering using piecewise smoothness priors: application to normal and abnormal electrocardiogram denoising, Signal Process. 133 (2017) 52–63, doi:10.1016/j.sigpro.2016.10.019.

[31] A. Mukherjee, A. Sengupta, Likelihood function modeling of particle filter in presence of non-stationary non-Gaussian measurement noise, Signal Process. 90 (6) (2010) 1873–1885, doi:10.1016/j.sigpro.2009.12.005.

[32] S. Meignen, D.-H. Pham, M.A. Colominas, On the use of short-time Fourier transform and synchrosqueezing-based demodulation for the retrieval of the modes of multicomponent signals, Signal Process. 178 (2021) 107760.

[33] V. Emiya, R. Hamon, C. Chaux, Being low-rank in the time-frequency plane, in: 2018 IEEE International Conference on Acoustics, Speech and Signal Processing (ICASSP), 2018, pp. 4659–4663, doi:10.1109/ICASSP.2018.8462423.

[34] K. Usevich, V. Emiya, D. Brie, C. Chaux, Characterization of finite signals with low-rank stft, in: 2018 IEEE Statistical Signal Processing Workshop (SSP), 2018, pp. 393–397, doi:10.1109/SSP.2018.8450745.

[35] D. Meng, F. De la Torre, Robust matrix factorization with unknown noise, in: 2013 IEEE International Conference on Computer Vision, 2013, pp. 1337–1344, doi:10.1109/ICCV.2013.169.

[36] A.S. Parihar, K. Singh, A study on Retinex based method for image enhancement, in: 2018 2nd International Conference on Inventive Systems and Control (ICISC), 2018, pp. 619–624.

[37] H. Rohilla, G. Asnani, K. Singh, A.S. Parihar, Low-light image enhancement using multi-exposure sequence generation and image fusion, Int. J. Adv. Sci. Technol. 29 (08) (2020) 4481–4490.

[38] H. Yong, D. Meng, W. Zuo, L. Zhang, Robust online matrix factorization for dynamic background subtraction, IEEE Trans. Pattern Anal. Mach. Intell. 40 (7) (2018) 1726–1740, doi:10.1109/TPAMI.2017.2732350.

[39] A.P. Dempster, N.M. Laird, D.B. Rubin, Maximum likelihood from incomplete data via the em algorithm, J. R. Stat. Soc. Ser. B 39 (1) (1977) 1–22, doi:10.1111/j.2517-6161.1977.tb01600.x.

[40] C.M. Bishop, Pattern Recognition and Machine Learning, Springer, 2006.

[41] R. Pinto, P. Engel, A fast incremental Gaussian mixture model, PLoS ONE 10 (10) (2015) e0141942.

[42] Y. Kim, K. Hong, H. Bang, Utilizing out-of-sequence measurement for ambiguous update in particle filtering, IEEE Trans. Aerosp. Electron. Syst. 54 (1) (2018) 493–501, doi:10.1109/TAES.2017.2741878.

[43] S.M. Mousavi, C.A. Langston, Hybrid seismic denoising using higher-order statistics and improved wavelet block thresholding, Bull. Seismol. Soc. Am. (2016). ssabull;0120150345v1

[44] J.K. Nielsen, T.L. Jensen, J.R. Jensen, M.G. Christensen, S.H. Jensen, Fast fundamental frequency estimation: making a statistically efficient estimator computationally efficient, Signal Process. 135 (2017) 188–197, doi:10.1016/j.sigpro.2017.01.011.

[45] L. Yu, H. Wu, J. Antoni, W. Jiang, Extraction and imaging of aerodynamically generated sound field of rotor blades in the wind tunnel test, Mech. Syst. Signal Process. 116 (2019) 1017–1028.